Liquidus Projection Surface and Isothermal Section at 1000 °C of the Co-Pr-B (Co-Rich) Ternary Phase Diagram*

*C.N. Christodoulou,** T.B. Massalski, and W.E. Wallace*
Department of Materials Science & Engineering
Carnegie Mellon University
Pittsburgh, PA 15213

The liquidus projection surface and the isothermal section at 1000 °C of the Co-Pr-B (Co-rich) ternary phase diagram have been determined. The binary and ternary intermetallics (Pr_2Co_{17}, $PrCo_5$, Pr_5Co_{19}, Pr_2Co_7, $PrCo_3$, $PrCo_2$, Co_3B, Co_2B, CoB, $Pr_2Co_{14}B$, $PrCo_4B$, $PrCo_{12}B$, $Pr_3Co_{11}B_4$, and $Pr_2Co_7B_3$) that were examined in the Co-rich portion of the Co-Pr-B ternary phase diagram were found to be true line compounds (no detectable solid solubility). The primary solidification phase field of the $Pr_2Co_{14}B$ intermetallic compound shares boundaries with the primary solidification phase fields of αCo, Pr_2Co_{17}, $PrCo_5$, $PrCo_4B$, and $PrCo_{12}B_6$ intermetallics. There are eight reactions associated with the $Pr_2Co_{14}B$ intermetallic compound: two ternary eutectic reactions (E_1 = Liquid ↔ $Pr_2Co_{14}B$ + $PrCo_{12}B_6$ + $PrCo_4B$ and E_2 = Liquid ↔ $Pr_2Co_{14}B$ + $PrCo_{12}B_6$ + αCo), two pseudobinary eutectic reactions (e_3 = Liquid ↔ $Pr_2Co_{14}B$ + $PrCo_4B$ and e_4 = Liquid ↔ $Pr_2Co_{14}B$ + $PrCo_{12}B_6$), three ternary quasi-peritectic reactions (P_1 = Pr_2Co_{17} + Liquid ↔ $Pr_2Co_{14}B$ + αCo, P_2 = Pr_2Co_{17} + Liquid ↔ $PrCo_5$ + $Pr_2Co_{14}B$, and P_3 = $Pr_2Co_{14}B$ + Liquid ↔ $PrCo_4B$ + $PrCo_5$), and one pseudobinary peritectic reaction (p_8 = Pr_2Co_{17} + Liquid ↔ $Pr_2Co_{14}B$). The composition of the magnetically important $Pr_2Co_{14}B$ intermetallic falls inside the primary solidification phase field of the Pr_2Co_{17} intermetallic. The reaction through which the $Pr_2Co_{14}B$ is produced is therefore the pseudobinary peritectic reaction Pr_2Co_{17} + Liquid ↔ $Pr_2Co_{14}B$. The $PrCo_{12}B_6$ and $PrCo_4B$ compounds are found to form congruently from the melt. At the temperature of 1000 °C and depending on the alloy composition, the $Pr_2Co_{14}B$ intermetallic can be found in solid-state thermodynamic equilibrium with one or two of the following phases: αCo, Pr_2Co_{17}, $PrCo_5$, $PrCo_4B$, and $PrCo_{12}B_6$. The obtained information about the Co-Pr-B phase diagram can be used to explain correctly all the phases present in the $Pr_2Co_{14}B$-based permanent magnets. The present work also emphasizes the extreme importance and usefulness of thermomagnetic measurements as an aid in the determination of phase diagrams that involve ferromagnetic phases.

1. Introduction

In alloy design, it is essential to have adequate information about the phase diagram of the elements involved. This is especially true in the case of processing permanent magnet materials where the kind of phases present and the final microstructure play an essential role in the resulting magnetic properties. In the present paper, the Co-Pr-B (Co-rich) phase diagram has been studied[1] in order to interpret the phases present and the microstructures obtained in the $Pr_2Co_{14}B$-based rapidly quenched[1-4] and sintered magnets.[1,5] Such magnets exhibit high intrinsic coercivities (5 to 25 kOe) and a high Curie temperature of 715 °C; they also exhibit an axis-to-plane spin reorientation phenomenon on heating at 410 °C, which causes the deterioration of the intrinsic coercivity above this temperature.[2]

In the present paper, the experimental results on the Co-Pr-B (Co-rich) ternary phase diagram are presented in terms of its liquidus projection surface and an isothermal section at 1000 °C.

2. Existing Information

Information in the form of general Co-R-B (R = rare earth) ternary phase diagram has been published previously, mainly in the limited form of relatively low-temperature isothermal sections,[6-15] as shown in Table 1. In the majority of the cases, the authors failed to point out the existence of the $R_2Co_{14}B$ phase,

*This research has been submitted by C.N. Christodoulou in partial fulfillment of the requirement for the degree of doctor of philosophy at Carnegie Mellon University.

**Present address: Mitsubishi Materials Corporation, Central Research Institute, 1-297 Kitabukuro-cho, Omiya, Saitama 330, Japan.

which at the time of their publication had not yet been discovered. A liquidus projection surface was published in the case of the Co-Gd-B system only,[10] but again the authors failed to recognize the existence of the primary solidification phase field of the $Gd_2Co_{14}B$ compound. Isothermal sections through the Co-Pr-B ternary phase diagram have been studied by Bilonizhko *et al.*[16] (at 400 and 600 °C) and by Chuang *et al.*[17-18] (at 700 °C). The isothermal section proposed by Bilonizhko *et al.*[16] appears to be partially incorrect because of the misplacement of the $Pr_2Co_{14}B$ intermetallic compound, which was misidentified as Pr_2Co_9B. As a result, they proposed several incorrect compatibility triangles (see "Appendix"), for example $Pr_2Co_9B + PrCo_4B + Pr_2Co_7$. Also, in the same isothermal section, the binary intermetallics Pr_5Co_{19} and Co_3B are missing.

Table 1 Existing R-Co-B (*R* = Rare Earth) Phase Diagrams

System	Isothermal section, °C	Liquidus projection surface	Reference
Pr-Co-B	700, 600, 400	No	16, 17, 18
Ce-Co-B	800, 400	No	6
Y-Co-B	800, 600	No	7
La-Co-B	600, 400	No	8
Gd-Co-B	800, 600	Yes	9, 10
Sm-Co-B	600, 400	No	11, 12
Nd-Co-B	600, 400	No	13
Dy-Co-B	800, 600	No	14
Er-Co-B	800, 600	No	14
Tb-Co-B	600	No	15

This additionally resulted in the choice of incorrect compatibility triangles like, for example, $Co + Co_2B + PrCo_{12}B_6$.

The Fe-Nd-B ternary phase diagram is the best known among the TM-R-B (TM = Co,Fe; R = rare earth) ternary phase diagrams.[19-24] An obvious difference between the Fe- and Co-based systems is the number of the intermetallic compounds present in the corresponding binaries with the rare earth elements. There are more binary intermetallic compounds in the Co-based system than in the Fe-based system. From this it can be expected that the Co-R-B ternary phase diagram will be considerably more complex than the Fe-R-B system. An important metallurgical feature of the Fe-Nd-B ternary phase diagram is the peritectic formation of the magnetically important $Nd_2Fe_{14}B$ intermetallic, according to the pseudobinary peritectic reaction:

$$Fe + \text{Liquid} \leftrightarrow Nd_2Fe_{14}B$$

This peritectic formation of the $Nd_2Fe_{14}B$ intermetallic is responsible for the fact that, in the fabrication of the $Nd_2Fe_{14}B$-based sintered magnets, the composition of the starting alloy has to be both Nd- and B-rich in order to fall inside the primary solidification phase field of $Nd_2Fe_{14}B$. When this happens, a very desirable microstructure can be produced during sintering, which results in magnets with high intrinsic coercivity. Also, the primary solidification phase field of $Nd_2Fe_{14}B$ extends towards the primary solidification phase field of Nd with which it shares a common boundary and forms a ternary eutectic at ~665 °C. This ternary eutectic involves $Nd_2Fe_{14}B$ with two other nonmagnetic phases (Nd and $NdFe_4B_4$). This feature

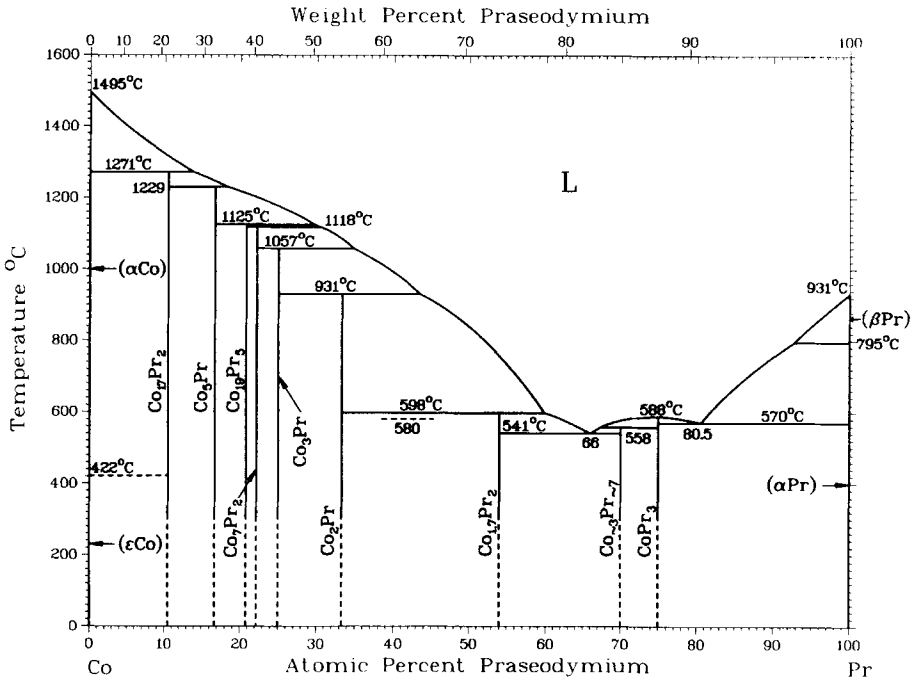

Fig. 1 Co-Pr binary phase diagram (reproduced from Ref. 25).

of the Fe-Nd-B phase diagram is found to be largely responsible for the doubling of the coercivity value of the $Nd_2Fe_{14}B$-based sintered magnets after annealing at the eutectic temperature. Annealing near this relatively low temperature produces equilibrium microstructures with smooth, defect-free, and isolated $Nd_2Fe_{14}B$ grains. This microstructure is found to be advantageous with regard to the magnetic properties of the $Nd_2Fe_{14}B$-based magnets. In the continuing exploration of TM-R-B systems, it became of interest to establish whether or not a similar low-temperature eutectic involving the $Pr_2Co_{14}B$ phase was also present in the Co-Pr-B ternary phase diagram. Here, Co is exchanged for Fe and Pr for Nd.

In the present work, comparisons are being made between the Co-Pr-B system with respect to Fe-Nd-B rather than Fe-Pr-B because the Fe-Pr-B phase diagram has not yet been determined. However, the Fe-Pr-B phase diagram is expected to be very similar to the Fe-Nd-B one. This is because the physical and chemical properties of Pr and Nd are very similar and also they form exactly the same binary and ternary compounds involving Fe and B. Furthermore, these compounds (Nd-Fe-B and Pr-Fe-B) have very similar magnetic properties.

2.1. Binary Phase Diagrams

2.1.1. Co-Pr Binary Phase Diagram

The Co-Pr binary phase diagram[25] is shown in Fig. 1. The Co-Pr binary intermetallics appear to be true line compounds. The structure and magnetic properties of the most important binary intermetallics are listed in Table 2. All of the Co-Pr intermetallics with Co concentration more than 50 at.% form peritectically according to the reactions:

p_1 : $\alpha Co + Liquid \leftrightarrow Pr_2Co_{17}$

p_2 : $Pr_2Co_{17} + Liquid \leftrightarrow PrCo_5$

p_3 : $PrCo_5 + Liquid \leftrightarrow Pr_5Co_{19}$

p_4 : $Pr_5Co_{19} + Liquid \leftrightarrow Pr_2Co_7$

p_5 : $Pr_2Co_7 + Liquid \leftrightarrow PrCo_3$

p_6 : $PrCo_3 + Liquid \leftrightarrow PrCo_2$

The intermetallics—$PrCo_2$, $PrCo_3$, Pr_2Co_7, Pr_5Co_{19}, and $PrCo_5$—can be described by the general formula[26-27] $PrCo_x$, where $x = (5|n|+4)/|n+2|$, $n = 0, 1, 2, 3$, and ∞, respectively. These compounds have been shown[26-28,30] to be one-dimensional, long-period superstructures of the $CaCu_5$-type structure. Khan[30] has shown that "n" is a measure of the number of double layers of the $PrCo_5$ type sandwiched between structural layers of the $PrCo_2$ type, so that for $n = 0$ one gets one of the Laves phase structures, and for $n \rightarrow \infty$ the formula is reduced to $PrCo_5$. In the case where "n" takes the negative values $n = -4, -6, -8, -9$, and $-\infty$, the $PrCo_{12}$, Pr_2Co_{17}, Pr_3Co_{22}, and $PrCo_7$ and $PrCo_5$ intermetallics can be derived from the above formula. Of these intermetallics, only the Pr_2Co_{17} and $PrCo_5$ are known to exist. A negative value of $n \leq -4$ also has a simple interpretation;[31] it measures through its reciprocal $2/|n|$, the fraction of Pr atoms in the $PrCo_5$ that must be replaced by Co atom pairs (aligned along the c axis) to obtain the structures of $PrCo_{12}$, Pr_2Co_{17}, etc. This structural interconnection of the Pr-Co binary intermetallics is generally applicable to all the Co-R (R = rare earth) binary intermetallics.

2.1.2. Co-B Binary Phase Diagram

The Co-B binary phase diagram[25] is shown in Fig. 2. The Co-B binary intermetallics appear to be true line compounds. The structure and the magnetic properties of the Co-B intermetallics are listed in Table 3. In the region with Co concentration exceeding 50 at.%, the Co_2B and CoB form congruently from the melt. There are also two eutectic reactions and one peritectic reaction:

e_1: $Liquid \leftrightarrow \alpha Co + Co_3B$

e_2: $Liquid \leftrightarrow Co_2B + CoB$

p_7: $Co_2B + Liquid \leftrightarrow Co_3B$

Table 2 Structure and Magnetic Properties of Pr-Co Binary Intermetallics

Phase	Easy direction of magnetization at *RT*	T_C, K	M_S at *RT*, μ_B/mole	Space group	Prototype	Lattice parameters, nm *a*	*c*	Reference
Pr_2Co_{17}	Plane	1177	31.9	$R\bar{3}m$	Th_2Zn_{17}	0.8455	1.2272	28, 29, this study
$PrCo_5$	Axis	912	9.95 (0 K)	*P6/mmm*	$CaCu_5$	0.5024	0.3990	26, 27, 29, this study
Pr_5Co_{19}	Axis	690	2.97	$R\bar{3}m$	Ce_5Co_{19}	0.5053	4.871	26, 27, 29
Pr_2Co_7.....	Axis	574	10.5	$P6_3/mmc$	Ce_2Ni_7	0.5060	3.652	26, 27, 29
$PrCo_3$	...	340	3.8 (0 K)	$R\bar{3}m$	$PuNi_3$	0.5062	2.481	26, 27, 29
$PrCo_2$	...	49	2.83 (0 K)	$Fd\bar{3}m$	$MgCu_2$	0.7312	...	26, 27, 29

Table 3 Structure and Magnetic Properties of Co-B Binary Intermetallics

Phase	Easy direction of magnetization at *RT*	T_C, K	M_S at *RT*, μ_B/mole	Space group	Prototype	Lattice parameters, nm *a*	*b*	*c*	Reference
Co_3B....	Plane	769	31.9	*Pnma*	Fe_3C	0.4411	0.5226	0.6631	31, this study
Co_2B....	Plane	425	9.95 (0 K)	*I4/mcm*	Al_2Cu	0.5015	...	0.4219	31, this study
CoB.....	...	Paramagnetic	2.97	*Pnma*	FeB	0.3948	0.5243	0.3037	31

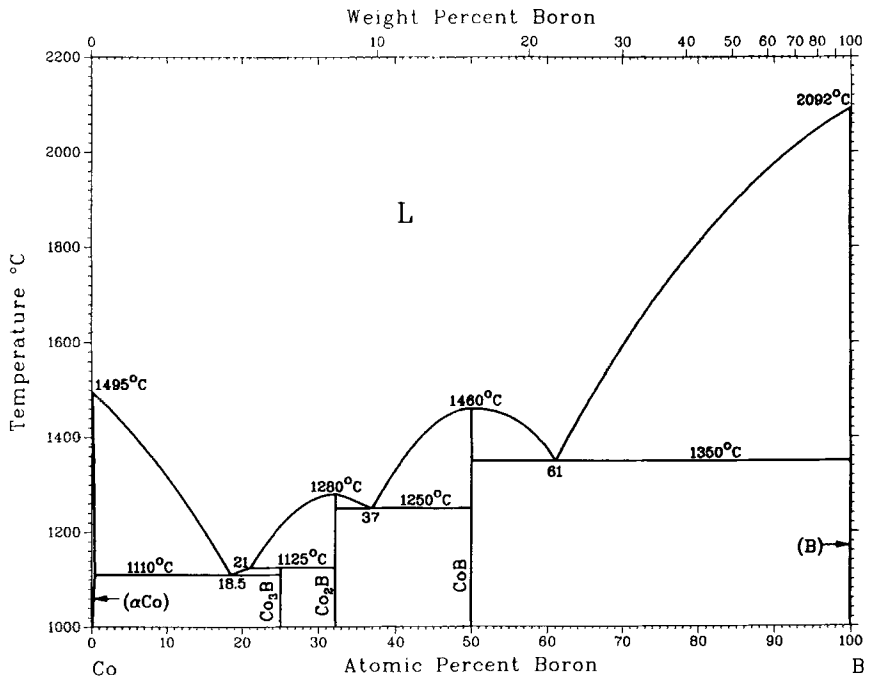

Fig. 2 Co-B binary phase diagram (reproduced from Ref. 25).

2.1.3. Pr-B Binary Phase Diagram

The Pr-B binary phase diagram[25] is shown in Fig. 3. All of the Pr-B binary intermetallics appear to be true line compounds with the exception of PrB_6, which exhibits considerable solid solubility. The Pr-B intermetallics do not come into the picture of the presently determined portion of the Co-Pr-B ternary phase diagram because only the Co-rich equilibria have been studied.

2.2. Pr-Co-B Ternary Intermetallics

The positions of the Pr-Co-B ternary intermetallics having Co concentration greater than 50 at.% are shown by crossed circles in Fig. 4. They are found to be true line compounds.[16] The most important ones, in terms of permanent magnets, are found to be $Pr_2Co_{14}B$, $PrCo_4B$, and $PrCo_{12}B_6$. The $Pr_2Co_{14}B$ intermetallic compound is of course the most important because it is magnetically uniaxial, exhibits a high anisotropy field (H_a = 100 kOe), and has a high Curie temperature (T_C = 715 °C). Therefore, this compound is a very good candidate as a constituent of permanent magnets.[1,2] By contrast, the $PrCo_4B$ phase is magnetically planar with a Curie temperature of 180 °C, while the $PrCo_{12}B_6$ phase is paramagnetic at room temperature with a Curie temperature of 167 K. The structures and magnetic properties of the Pr-Co-B intermetallics[32-39] are summarized in Table 4.

3. Experimental Details

More than 60 alloy compositions were selected in order to construct the liquidus projection surface and the isothermal section at 1000 °C of the Co-Pr-B (Co-rich) phase diagram. The alloy compositions were spread in the Co-rich region of the phase diagram concentrating particularly around the composition $Pr_2Co_{14}B$ and its suspected primary solidification phase field, as shown in Fig. 4. Some of the alloy compositions were chosen in order to fall inside the suspected two- or three-phase fields. A few of the compositions of the prepared ternary Pr-Co-B alloys are listed in Table 5. The as-cast alloys have been prepared by induction melting of the constituent elements (greater than 99.9 wt.% purity) in a water-cooled copper boat, under the flow of ultrapure argon gas. The ingots were remelted at least five times to ensure a complete melt and mixing of the individual elements. In this way, high quality ingots of approximately 3 g in weight were produced. The elemental losses using this method were essentially nil, and no visible surface oxidation of the alloys has been observed.

Each of the as-cast ingots was cut into two pieces, and one piece (~1.5 g) was subsequently wrapped in tantalum foil and encapsulated in quartz tubes under 0.5 atm of argon gas. These samples were heat treated isothermally at 1000 °C for about 10 weeks and then quenched into water. The quality of the alloys after heat treatment was very good. No surface oxidation was observed, and all samples retained their original shape.

Both pieces of each ingot (the as-cast and the isothermally heat treated at 1000 °C) were carefully studied, in terms of the phases present, by using thermomagnetic (TMA) measurements, X-ray diffraction (XRD), microhardness analysis, and microstructural observation. TMA data have been obtained using a vibrating sample magnetometer (VSM) at temperatures of 77 K up to 25 °C and a Faraday balance for temperatures be-

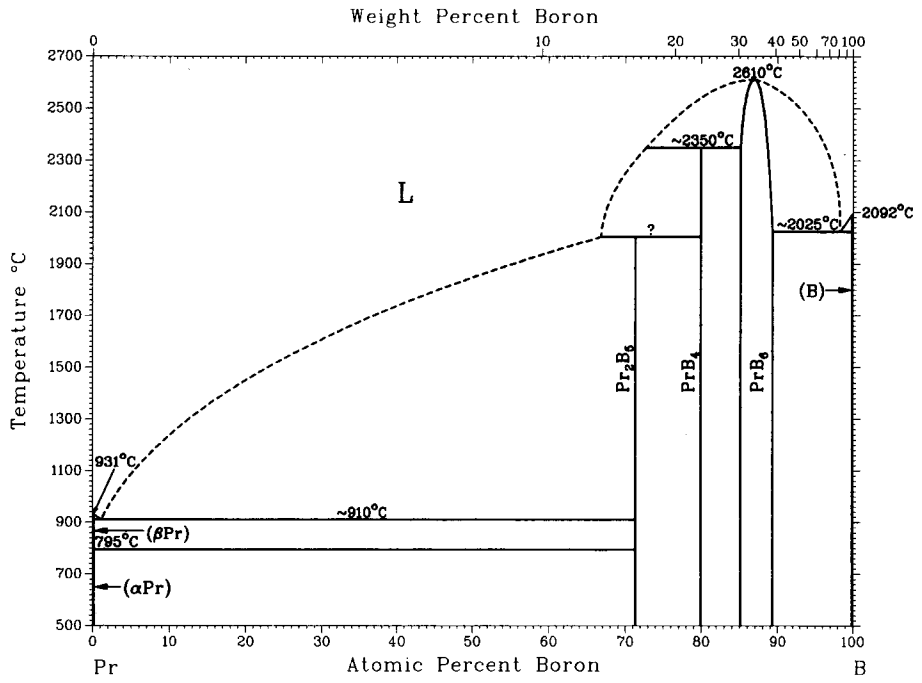

Fig. 3 Pr-B binary phase diagram (reproduced from Ref. 25).

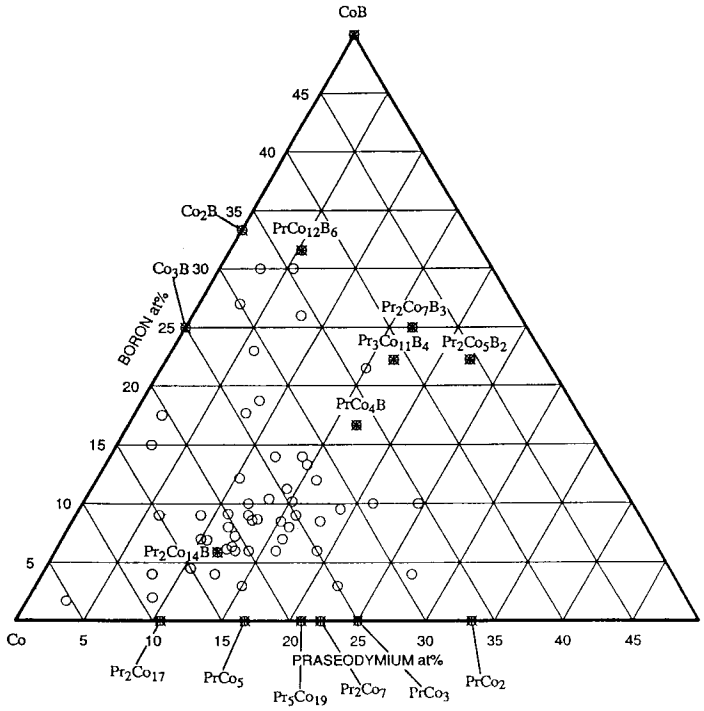

Fig. 4 Compositions of the alloys (open circles) studied for determining the isothermal section at 1000 °C of the Co-Pr-B (Co-rich) ternary phase diagram. The existing binary and ternary intermetallics are represented by crossed circles.

tween 25 °C and 1050 °C. A diffractometer with a theta-theta wide angle goniometer was used for X-ray experiments. Copper radiation (CuK_α) and a graphite monochromator were used to obtain the X-ray powder diffraction patterns. A differ-

Table 4 Structure and Magnetic Properties of Pr-Co-B Intermetallics

Phase	Easy direction of magnetization at *RT*	T_C, K	Ms at *RT*, emu/g	Space group	Prototype	Lattice parameters, nm *a*	c	Reference
$Pr_2Co_{14}B$.....	Axis	988	106	$P4_2/mnm$	$Nd_2Fe_{14}B$	0.8657	1.1896	28, 29, this study
$PrCo_4B$.....	Plane	455	45	$P6/mmm$	$CeCo_4B$	0.5118	0.6892	26, 27, 29, this study
$PrCo_{12}B_6$.....	Paramagnetic	167	32 (77 K)	$R\bar{3}m$	$SrNi_{12}B_6$	0.9484	0.7475	26, 27, 29, this study
$Pr_3Co_{11}B_4$...	Cone	411	30	$P6/mmm$	$Ce_3Co_{11}B_4$	0.5147	0.9785	26, 27, 29
$Pr_2Co_7B_3$.....	Cone	323	19	$P6/mmm$	$Ce_2Co_7B_3$	0.5150	1.2750	26, 27, 29

Table 5 Composition of Few Alloys Used for the Determination of the Co-Pr-B Phase Diagram

Sample #	Composition, at.% Pr	Co	B	Chemical formula	Symbol
1.....	11.77	82.35	5.88	$Pr_2Co_{14}B$	A_1
2.....	16.67	66.66	16.66	$PrCo_4B$	...
3.....	5.26	63.16	31.58	$PrCo_{12}B_6$	...
4.....	16.67	61.11	22.22	$Pr_3Co_{11}B_4$	...
5.....	16.67	58.33	25	$Pr_2Co_7B_3$	...
6.....	10.53	89.47	...	Pr_2Co_{17}	...
7.....	16.67	83.33	...	$PrCo_5$	...
8.....	...	75	25	Co_3B	...
9.....	...	66.67	33.33	Co_2B	...
10.....	9	89	2	...	I_1
11.....	6	85	9	...	I_2, A_3
12.....	5.45	64.55	30	...	I_3, A_4
13.....	15	82	3	...	I_4
14.....	12.5	83.5	4	...	I_5
15.....	2.89	95.42	1.69	...	A_2
16.....	12.99	78.43	8.58	...	A_5

ential thermal analyzer capable of reaching temperatures up to 1450 °C was employed in order to find the temperatures where melting occurs in some of the alloys.

4. Experimental Results

4.1. Co-Pr-B (Co-Rich) Isothermal Section at 1000 °C

The experimentally determined Co-Pr-B (Co-rich) isothermal section at 1000 °C is shown in Fig. 5. The binary and ternary Pr-Co-B intermetallics were found to be true line compounds (no detectable solid solubility). This result is in agreement with the results obtained by other researchers,[16-18,39] and it was confirmed by obtaining XRD patterns from several out-of-stoichiometry alloys, which contained these intermetallics. In the case of the $Pr_2Co_{14}B$ intermetallic compound, the lattice parameters determined for such out-of-stoichiometry alloys were the same as those determined for the stoichiometric compound itself (a = 0.866 nm and c = 1.190 nm) within the experimental error of ±0.001 nm. In addition, the Curie temperature of the $Pr_2Co_{14}B$ compound present in the out-of-stoichiometry alloys was the same (T_C = 715 °C) as the Curie temperature obtained for the single-phase stoichiometric compound within the experimental error of ±3 °C. The lattice parameters and Curie temperature are generally sensitive to changes in the chemical composition. Since no such changes were observed, it was concluded that no appreciable solid solubility exists in the $Pr_2Co_{14}B$ intermetallic compound. This result agrees with a similar study reported by Buschow *et al.*[22] for the $Nd_2Fe_{14}B$ prototype compound. Similar experiments have confirmed that all of the Pr-Co-B ternary intermetallics that were examined ($Pr_2Co_{14}B$, $PrCo_4B$, $PrCo_{12}B_6$, $Pr_3Co_{11}B_4$, and $Pr_2Co_7B_3$) have no appreciable solid solubility.

In addition to the fact that the binary and ternary Pr-Co-B (Co-rich) intermetallics are true line compounds, it was also found that no liquid exists in equilibrium with the $Pr_2Co_{14}B$ phase below 1000 °C (only solid phases). Therefore, in the isothermal section shown in Fig. 5, the single-phase fields are represented by points (the composition of the intermetallics), the two-phase fields by straight lines (lines linking the compositions of two intermetallics), and the three-phase fields by triangles. These triangles are "compatibility triangles," and their three sides are Alkemade lines (see "Appendix"). Liquid phase exists in the vicinity of the $PrCo_2$ binary intermetallic only, and this can be verified from the Pr-Co binary phase diagram in Fig. 1. Thermomagnetic analysis (TMA) and X-ray powder diffraction patterns (random and aligned in 15 kOe magnetic field) have been obtained for $Pr_2Co_{14}B$, $PrCo_4B$, $PrCo_{12}B_6$, Pr_2Co_{17}, $PrCo_5$, Co_3B, and Co_2B single phases in order to serve as "standards" for the detection of these phases when they were present in mixtures. These TMA patterns are shown in Fig. 6, and X-ray patterns are shown in Fig. 7 through 9. The TMA curve (Fig. 6, line g) of $Pr_2Co_{14}B$ shows a "spike" type of transition at 410 °C. This is due to the axis-to-plane spin reorientation exhibited by the $Pr_2Co_{14}B$ phase. This transition is so profound in the TMA curve that its occurrence could be taken as unambiguous evidence of the presence of the $Pr_2Co_{14}B$ phase in the alloy under consideration. Aligned powders of magnetically axial compounds, such as $Pr_2Co_{14}B$ and $PrCo_5$, exhibit diffraction patterns with enhanced (00*l*) intensities and diminished (*hk*0) intensities (compared to the

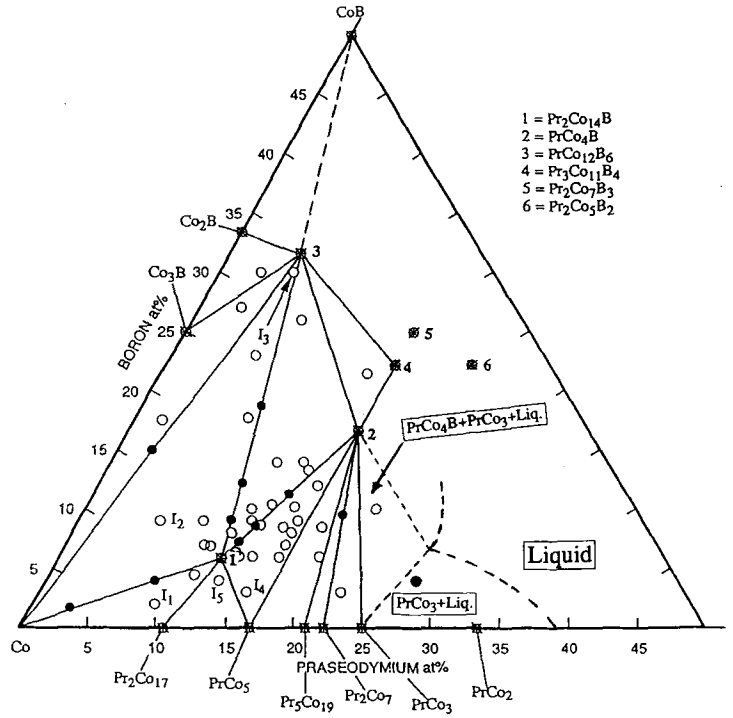

Fig. 5 Isothermal section at 1000 °C of the Co-Pr-B (Co-rich) ternary phase diagram. The single-phase, two-phase, and three-phase regions are represented by crossed circles, solid circles, and open circles, respectively. Dashed lines represent hypothetical isothermal phase boundaries.

random powders diffraction pattern). On the other hand, magnetically planar compounds, such as $PrCo_4B$, Pr_2Co_{17}, Co_3B, and Co_2B, exhibit diffraction patterns with enhanced (*hk*0) intensities and diminished (00*l*) intensities.

The $Pr_2Co_{14}B$ intermetallic is involved in five compatibility triangles with αCo, Pr_2Co_{17}, $PrCo_5$, $PrCo_4B$, and $PrCo_{12}B_6$, respectively as shown in Fig. 5. The microstructures of five isothermally heat treated alloys (I_1, I_2, I_3, I_4, and I_5), whose compositions (Fig. 5) fall inside some of these compatibility triangles, are shown in Fig. 10 through 14. Each of the microstructures shown in these figures is accompanied by the corresponding TMA curve. The TMA curve of the alloy confirms the chemical compositions of the phases present in the alloy. This is indicated by the occurrence of the Curie temperatures corresponding to these phases (compare with the standard TMA curves of Fig. 6). For example, Fig. 10 shows the microstructure of alloy I_1 of composition $Pr_9Co_{89}B_2$, which was isothermally heat treated at 1000 °C. It also shows the TMA curve for the same alloy. The TMA curve (Fig. 10b) suggests that alloy I_1 consists of three phases: $Pr_2Co_{14}B$ (T_C = 715 °C), Pr_2Co_{17} (T_C = 904 °C), and αCo (T_C = 1127 °C). The T_C of αCo is not evident in the TMA curve because the maximum temperature that the instrument could reach was only 1050 °C. However, the nonzero value of the magnetization at the maximum temperature of measurement was taken as evidence of the existence of Co. This is because there is no compound in the Co-Pr-B system, other than αCo, that has Curie temperature higher than that of Pr_2Co_{17} (T_C = 904 °C). The three phases ($Pr_2Co_{14}B$, Pr_2Co_{17}, αCo) identified by the TMA are also shown in the microstructure of the alloy shown in Fig.

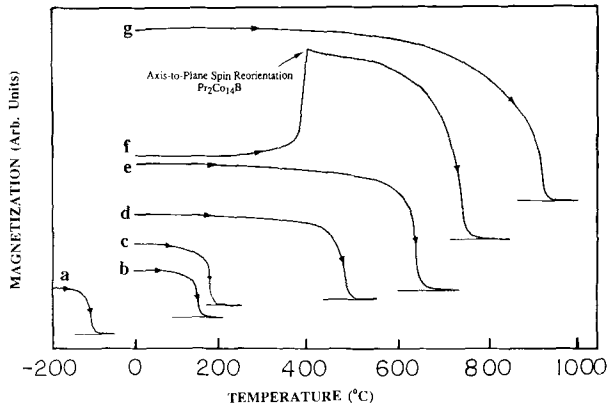

Fig. 6 Standard thermomagnetic analysis (TMS) curves of single phases: (a) $PrCo_{12}B_6$ (T_C = 167 K), (b) Co_2B (T_C = 152 °C), (c) $PrCo_4B$ (T_C = 180 °C), (d) Co_3B (T_C = 496 °C), (e) $PrCo_5$ (T_C = 639 °C), (f) $Pr_2Co_{14}B$ (T_C = 715 °C), and (g) Pr_2Co_{17} (T_C = 904 °C). The $Pr_2Co_{14}B$ phase also shows an axis-to-plane spin reorientation at 410 °C (spike).

10a. The composition of alloy I_1 falls inside the compatibility triangle comprised of the $Pr_2Co_{14}B$, Pr_2Co_{17}, and αCo phases. Therefore, following the solidification under equilibrium conditions, one expects to find the above three phases present in the alloy.

The microstructures and corresponding TMA curves (Fig. 11-14) of the alloys heat treated isothermally at 1000 °C—I_2

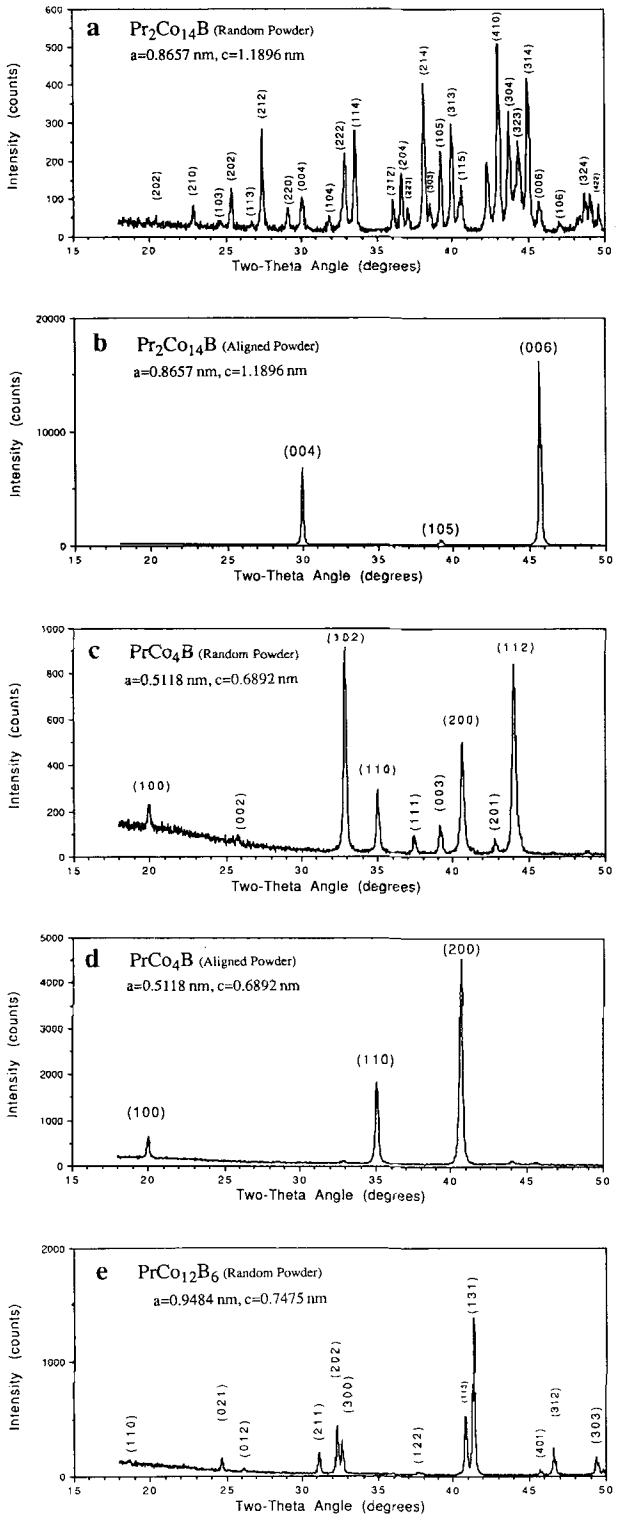

Fig. 7 X-ray powder diffraction patterns (CuK_α) of the single phases—$Pr_2Co_{14}B$, $PrCo_4B$, and $PrCo_{12}B_6$. (a,c,e) = Random. (b,d) = Aligned in magnetic field of 15 kOe.

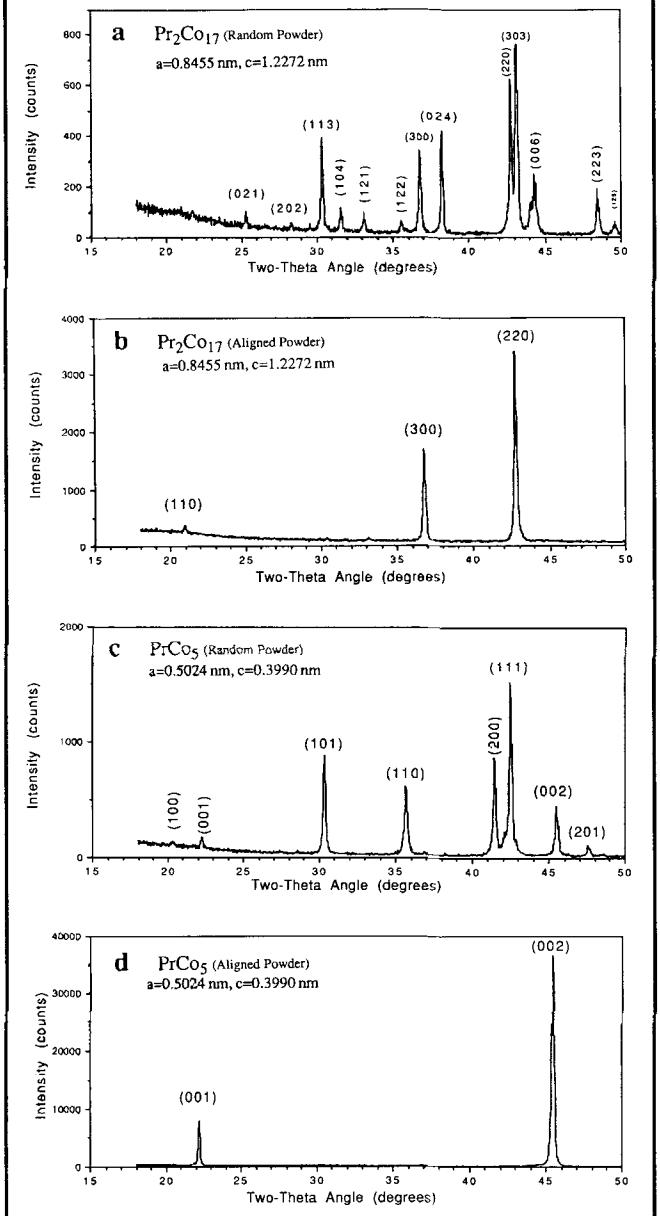

Fig. 8 X-ray powder diffraction patterns (CuK_α) of the single phases Pr_2Co_{17} and $PrCo_5$. (a,c) = Random. (b,d) = Aligned in magnetic field of 15 kOe.

($Pr_6Co_{85}B_9$), I_3 ($Pr_{5.45}Co_{64.55}B_{30}$), I_4 ($Pr_{15}Co_{82}B_3$), and I_5 ($Pr_{12.5}Co_{83.5}B_4$)—can be interpreted in a similar manner by considering the compatibility triangles inside which these alloy compositions are located.

The existence of compatibility triangles involving $Pr_2Co_{14}B$, and the phases such as αCo, Pr_2Co_{17}, $PrCo_5$, $PrCo_4B$, and $PrCo_{12}B_6$, is very important in alloy design. If one wants to prepare an alloy consisting mainly of $Pr_2Co_{14}B$ together with two other phases (αCo, Pr_2Co_{17}, $PrCo_5$, $PrCo_4B$, or $PrCo_{12}B_6$), this can be done by solidification under equilibrium conditions of an initial melt of a composition falling into the compatibility triangle comprised of the desired phases. If a two-phase alloy is desired ($Pr_2Co_{14}B$ together with one of the

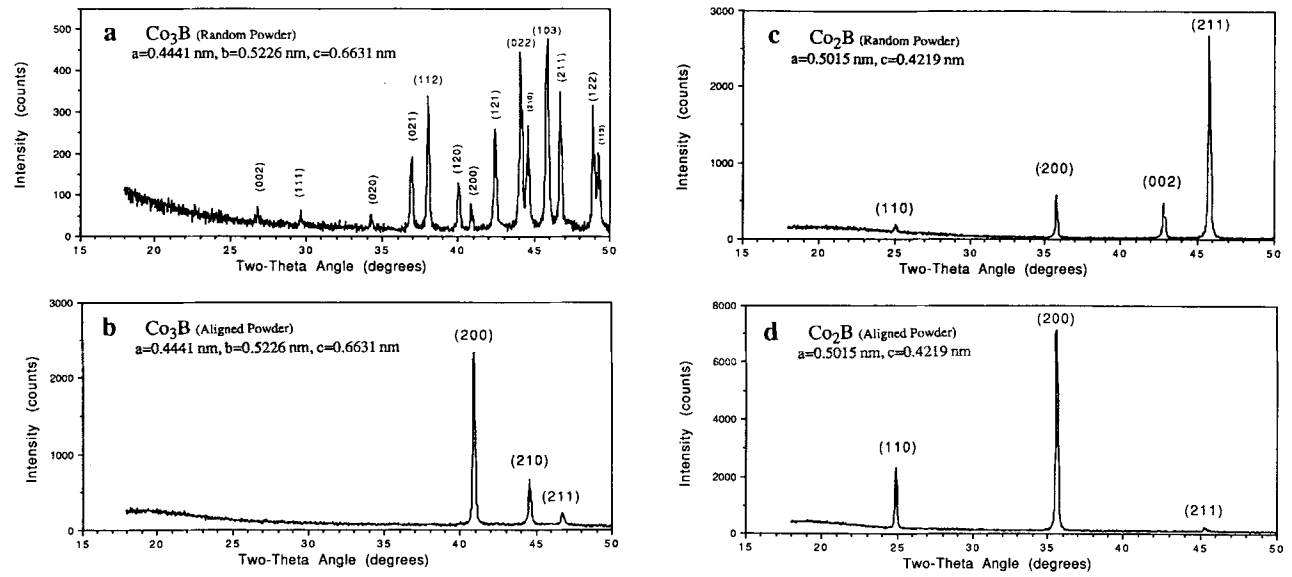

Fig. 9 X-ray powder diffraction patterns (CuK_α) of the single phases Co_3B and Co_2B. (a,c) = Random. (b,d) = Aligned in magnetic field of 15 kOe.

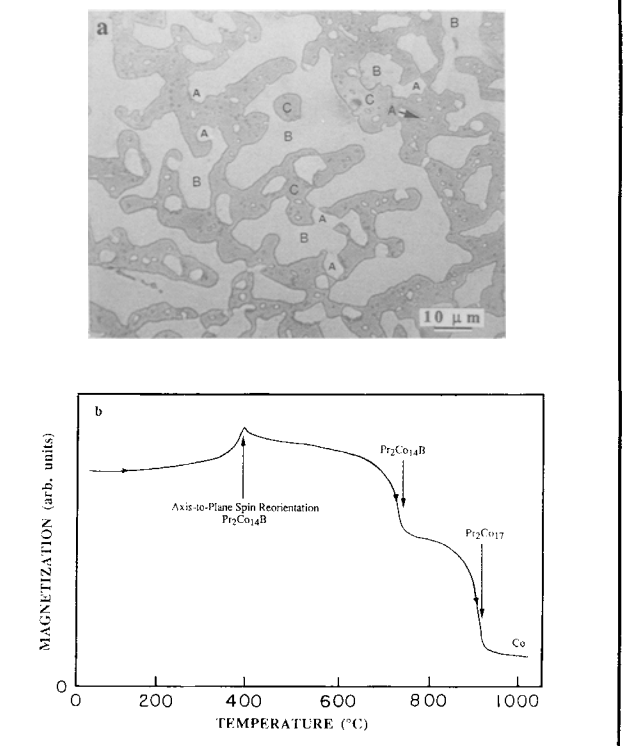

Fig. 10 Microstructure (a) and TMA (b) of the isothermally heat treated at 1000 °C alloy I_1 ($Pr_9Co_{89}B_2$). A = Co, B = Pr_2Co_{17}, C = $Pr_2Co_{14}B$.

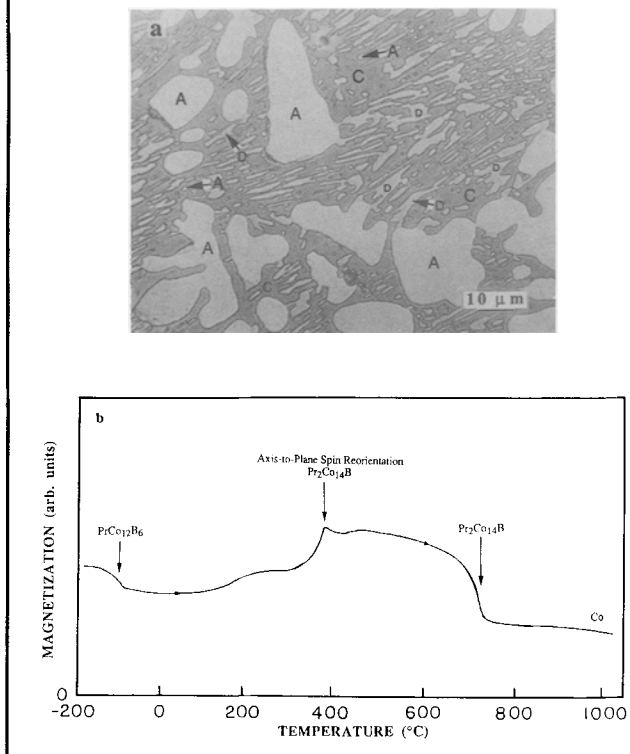

Fig. 11 Microstructure (a) and TMA (b) of the isothermally heat treated at 1000 °C alloy I_2 ($Pr_6Co_{85}B_9$). A = Co, C = $Pr_2Co_{14}B$, D = $PrCo_{12}B_6$.

other phases), then the composition of the melt has to be on the Alkemade line between the $Pr_2Co_{14}B$ and the second desired phase. The above observations can be used as a guide in choosing the compositions of the alloys used for fabrication of the permanent magnets. Also, the information about the existing Alkemade lines was very useful in applying the Alkemade theorem (see "Appendix") in order to determine the Co-Pr-B (Co-rich) liquidus projection, which is described below.

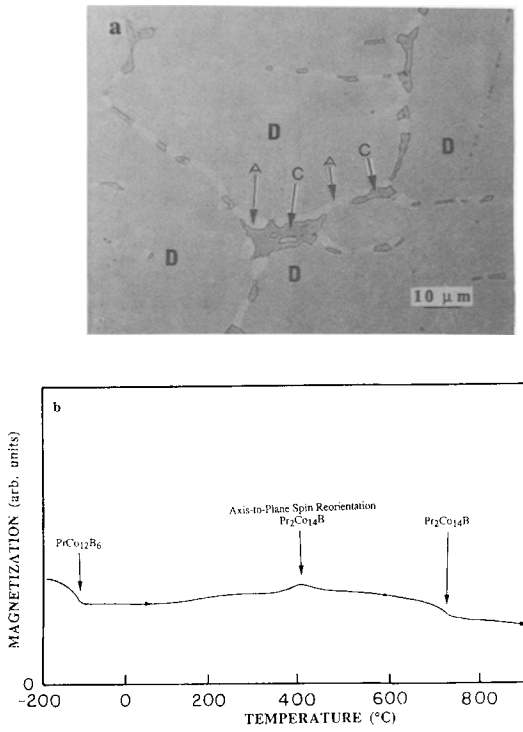

Fig. 12 Microstructure (a) and TMA (b) of the isothermally heat treated at 1000 °C alloy I_3 ($Pr_{5.45}Co_{64.55}B_{30}$). A = Co, C = $Pr_2Co_{14}B$, D = $PrCo_{12}B_6$.

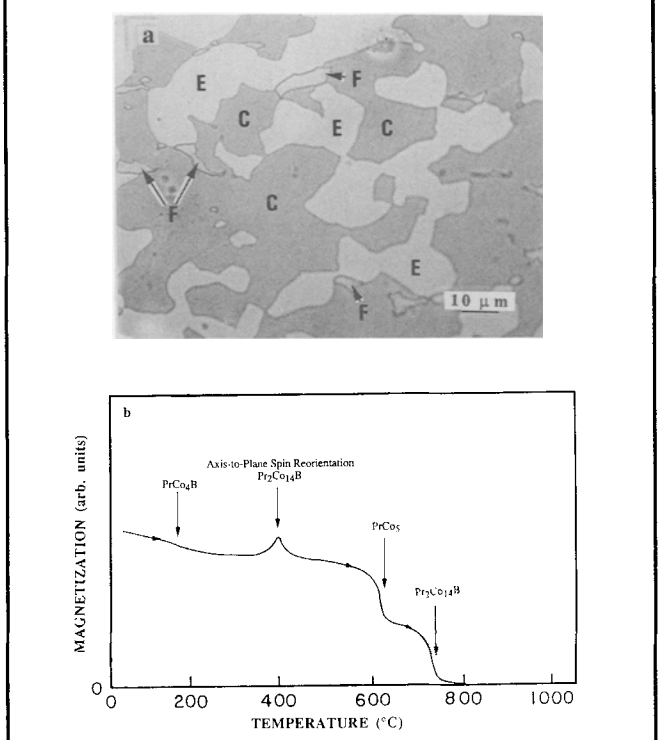

Fig. 13 Microstructure (a) and TMA (b) of the isothermally heat treated at 1000 °C alloy I_4 ($Pr_{15}Co_{82}B_3$). C = $Pr_2Co_{14}B$, E = $PrCo_5$, F = $PrCo_4B$.

4.2. Co-Pr-B (Co-Rich) Liquidus Projection Surface

The experimentally determined liquidus projection surface of the Co-Pr-B (Co-rich) ternary phase diagram is shown in Fig. 15. The $PrCo_4B$ and $PrCo_{12}B_6$ intermetallics appear to form congruently from the melt, as was suggested by the TMA, XRD, and microstructures of the respective as-cast alloys that were found to be single-phase alloys. The melting points, as determined by the DTA heating curves, are 1100 °C for the $PrCo_4B$ and 1290 °C for the $PrCo_{12}B_6$. The composition of the $Pr_2Co_{14}B$ intermetallic falls inside the primary solidification phase field of Pr_2Co_{17} and appears to form peritectically at approximately 1120 °C according to the pseudobinary peritectic reaction:

$$Pr_2Co_{17} + \text{Liquid} \leftrightarrow Pr_2Co_{14}B$$

The primary solidification phase field of $Pr_2Co_{14}B$ has boundaries in common with five other primary solidification phase fields: Co, Pr_2Co_{17}, $PrCo_5$, $PrCo_4B$, and $PrCo_{12}B_6$. This is a consequence of the fact that $Pr_2Co_{14}B$ forms Alkemade lines with the above phases.

4.2.1. Ternary Invariant Reactions

There are a number of ternary invariant reactions in this portion of the phase diagram of which 12 appear to be the most important. Eight of them are ternary quasi-peritectic reactions labeled as "P," and four are ternary eutectic reactions labeled as "E." These are listed below.

Ternary quasi-peritectic reactions are:

$$P_1: Pr_2Co_{17} + \text{Liquid} \leftrightarrow Pr_2Co_{14}B + \alpha Co$$

$$P_2: Pr_2Co_{17} + \text{Liquid} \leftrightarrow PrCo_5 + Pr_2Co_{14}B$$

$$P_3: Pr_2Co_{14}B + \text{Liquid} \leftrightarrow PrCo_4B + PrCo_5$$

$$P_4: Co_2B + \text{Liquid} \leftrightarrow Co_3B + PrCo_{12}B_6$$

$$P_5: PrCo_5 + \text{Liquid} \leftrightarrow Pr_5Co_{19} + PrCo_4B$$

$$P_6: Pr_5Co_{19} + \text{Liquid} \leftrightarrow Pr_2Co_7 + PrCo_4B$$

$$P_7: Pr_2Co_7 + \text{Liquid} \leftrightarrow PrCo_3 + PrCo_4B$$

$$P_8: PrCo_3 + \text{Liquid} \leftrightarrow PrCo_2 + PrCo_4B$$

Three of the above ternary quasi-peritectic reactions (P_1, P_2, and P_3) involve the $Pr_2Co_{14}B$ phase.

Ternary eutectic reactions are:

$$E_1: \text{Liquid} \leftrightarrow Pr_2Co_{14}B + PrCo_{12}B_6 + PrCo_4B$$

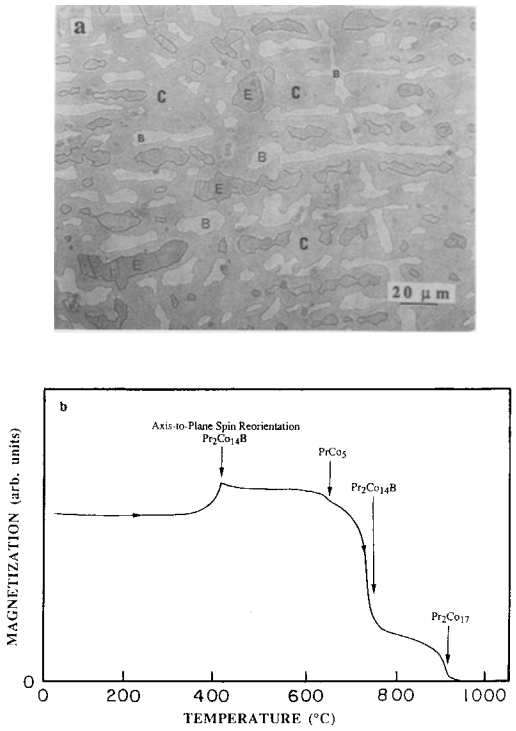

Fig. 14 Microstructure (a) and TMA (b) of the isothermally heat treated at 1000 °C alloy I_5 ($Pr_{12.5}Co_{83.5}B_4$). B = Pr_2Co_{17}, C = $Pr_2Co_{14}B$, E = $PrCo_5$.

E_2: Liquid ↔ $Pr_2Co_{14}B + PrCo_{12}B_6 + \alpha Co$

E_3: Liquid ↔ $PrCo_{12}B_6 + Co_3B + \alpha Co$

E_4: Liquid ↔ $PrCo_{12}B_6 + Co_2B + CoB$

Two of the above ternary eutectic reactions (E_1 and E_2) involve the $Pr_2Co_{14}B$ phase.

4.2.2. Ternary Univariant Reaction Boundaries

In the composition region with Co concentrations exceeding 50 at.%, there are six univariant reaction boundaries; one is a peritectic type (pseudobinary peritectic) and five are eutectic types (pseudobinary eutectic). The intersections between the univariant reaction boundaries and the Alkemade lines between the compositions of the two intermetallics involved represent the maximum temperature on those boundaries. These intersections are labeled as "p" for the peritectic type and "e" for the eutectic type. The peritectic-type univariant reaction boundaries are also known as alteration boundaries. The reactions occurring on the univariant reaction boundaries are listed below. In front of each reaction, the label of the maximum temperature (on the boundaries, Fig. 15) is also indicated.

Pseudobinary peritectic reaction is:

p_8: Pr_2Co_{17} + Liquid ↔ $Pr_2Co_{14}B$

This reaction is very important because it produces the $Pr_2Co_{14}B$ phase, which is magnetically hard and is responsible

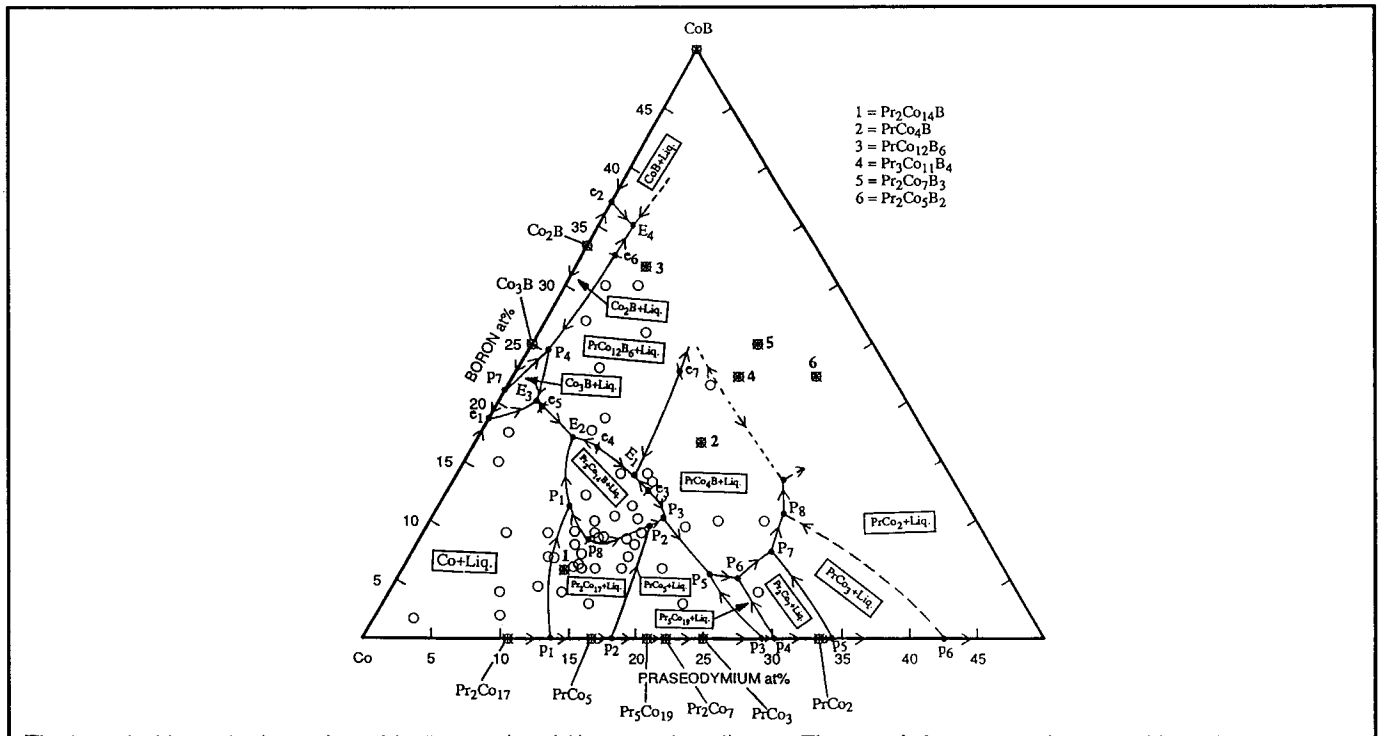

Fig. 15 Liquidus projection surface of the Co-Pr-B (Co-rich) ternary phase diagram. The open circles represent the compositions of the alloys studied. Dashed lines represent hypothetical phase boundaries. p_1-p_7 = binary peritectics, p_8 = pseudobinary peritectic boundary, P_1-P_8 = ternary quasi-peritectics, e_1-e_2 = binary eutectics, e_3-e_7 = pseudobinary eutectic boundaries, E_1-E_4 = ternary eutectics.

for the high intrinsic coercivities obtained in the Pr-Co-B permanent magnets.

Pseudobinary eutectic reactions are:

e_3: Liquid ↔ $Pr_2Co_{14}B + PrCo_4B$

e_4: Liquid ↔ $Pr_2Co_{14}B + PrCo_{12}B_6$

e_5: Liquid ↔ $PrCo_{12}B_6 + \alpha Co$

e_6: Liquid ↔ $PrCo_{12}B_6 + Co_2B$

e_7: Liquid ↔ $PrCo_{12}B_6 + PrCo_4B$

Two of the above pseudobinary eutectic reactions (e_3 and e_4) involve the $Pr_2Co_{14}B$ phase.

4.2.3. Alloy Microstructures

Microstructures have been obtained for all of the as-cast alloys. The initial "nonequilibrium microstructure" of the as-cast alloys provides information about the primary solidification phase fields and other important features of the phase diagram, like eutectic and peritectic reactions, etc. Subsequent equilibrium microstructures do not necessarily provide this information because they only reveal the end products. However, they are very useful in determining compatibility triangles and Alkemade lines as was described in section 4.1.

In this section, a representative sample of microstructures is presented to illustrate the most important features of the Co-Pr-B phase diagram. Each of the above selected microstructures is accompanied by the TMA curve of the corresponding alloy. As described in section 4.1, the TMA curves could be interpreted in terms of the chemical compositions of the phases present in the alloy. For some alloys, both the heating and cooling TMA curves were obtained in the range of temperature between 20 and 1000 °C. Upon heating, the TMA curve of the sample reveals the phases present. When an as-cast alloy is heated at ~1000 °C, some of the phases may begin dissolving to form other phases. Therefore, upon cooling, the TMA curve will reveal if such changes occurred and also what kind of phases were involved. This type of interpretation is elucidated in more detail below, where some microstructures in conjunction with the TMA curves will be presented. The selected microstructures of the as-cast alloys will be described in relation to the liquidus projection surface of the Co-Pr-B phase diagram, as shown in Fig. 16. The compositions of the selected as-cast alloys A_1 ($Pr_2Co_{14}B$), A_2 ($Pr_{2.89}Co_{95.42}B_{1.69}$), A_3 ($Pr_6Co_{85}B_9$), A_4 ($Pr_{5.45}Co_{64.55}B_{30}$), and A_5 ($Pr_{12.99}Co_{78.43}B_{8.58}$) are also shown on the above projection.

Alloy A_1 of Composition $Pr_2Co_{14}B$. The melt of alloy A_1 solidifies along the Pr_2Co_{17}-A_1 line by precipitating the primary Pr_2Co_{17} until the remaining liquid reaches the pseudobinary peritectic point p_8 (~1120 °C). At that point, the Pr_2Co_{17} crystals react with the liquid of composition p_8 to form peritectically the $Pr_2Co_{14}B$ according to the reaction:

Pr_2Co_{17} + Liquid ↔ $Pr_2Co_{14}B$

The peritectic structure-type of microstructure with the $Pr_2Co_{14}B$ phase forming around the Pr_2Co_{17} crystals is clearly

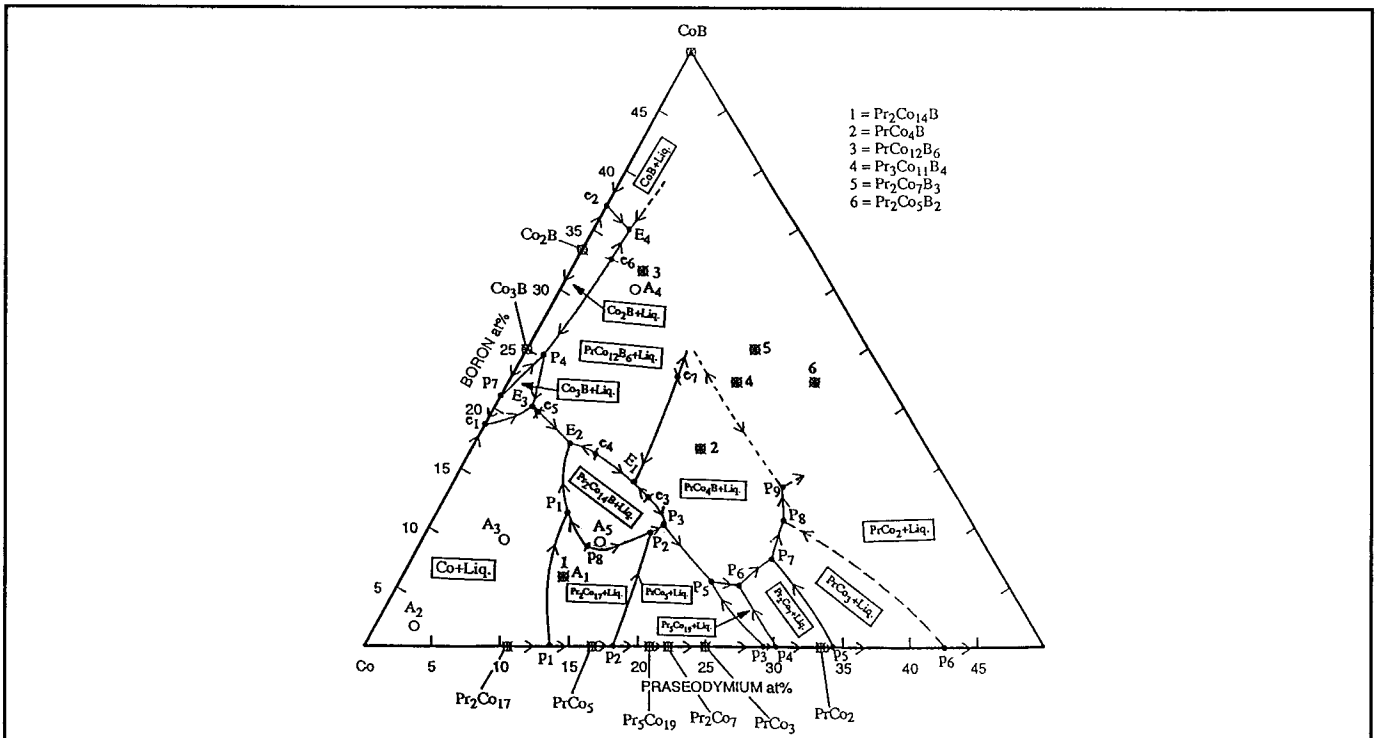

Fig. 16 Liquidus projection surface of the Co-Pr-B (Co-rich) ternary phase diagram. The compositions of the alloys—A_1 = $Pr_2Co_{14}B$, A_2 = $Pr_{2.89}Co_{95.42}B_{1.69}$, A_3 = $Pr_6Co_{85}B_9$, A_4 = $Pr_{5.45}Co_{64.55}B_{30}$, and A_5 = $Pr_{12.99}Co_{78.43}B_{8.58}$—are represented by open circles.

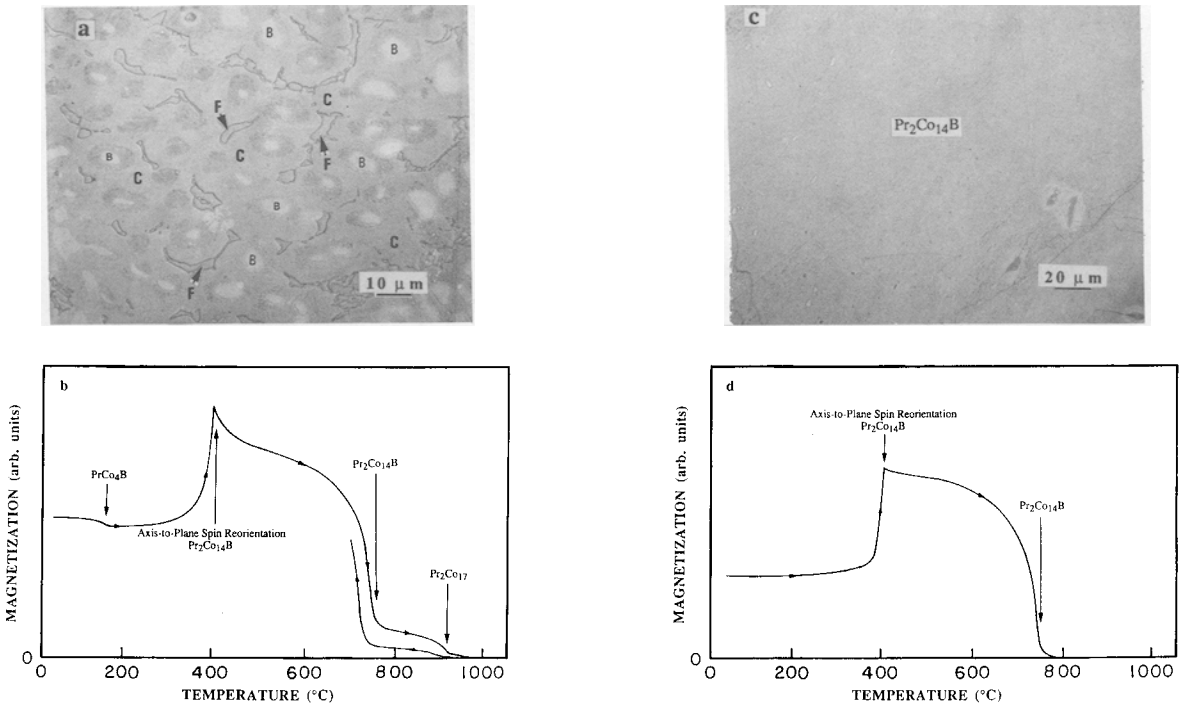

Fig. 17 Microstructure (a) and TMA (b) of the as-cast alloy A_1 ($Pr_2Co_{14}B$). Microstructure (c) and TMA (d) of the alloy A_1 heat treated at 1000 °C. B = Pr_2Co_{17}, C = $Pr_2Co_{14}B$, F = $PrCo_4B$.

seen in Fig. 17a. Under equilibrium conditions, all of the Pr_2Co_{17} crystals should be dissolved, and a single-phase ($Pr_2Co_{14}B$) alloy should be produced. In general, however, the as-cast conditions of cooling correspond to nonequilibrium conditions because of kinetic considerations. Hence, some of the Pr_2Co_{17} primary crystals remain undissolved, and they show up in the microstructure. The unavailability of Pr_2Co_{17} crystals to react with the liquid (because they are covered by a newly formed layer of $Pr_2Co_{14}B$ phase) forces the remaining liquid of composition p_8 to solidify independently. The composition of the liquid follows the $Pr_2Co_{14}B$-p_8 line through the $Pr_2Co_{14}B$ primary solidification phase field where primary $Pr_2Co_{14}B$ precipitates. It finally reaches the equilibrium boundary of the primary solidification phase field of $PrCo_4B$, where some secondary $PrCo_4B$ crystals form. The $PrCo_4B$ crystals are shown (Fig. 17a) in the form of "islands" squeezed between the $Pr_2Co_{14}B$ phase.

The TMA heating curve (Fig. 17b) of the as-cast alloy A_1 confirms the presence of the three phases in the alloy $Pr_2Co_{14}B$ (T_C = 715 °C), Pr_2Co_{17} (T_C = 904 °C), and $PrCo_4B$ (T_C = 180 °C). The "spike" type of transition at approximately 410 °C is due to the earlier mentioned axis-to-plane spin reorientation transition occurring upon heating the $Pr_2Co_{14}B$ phase. The presence of such a transition in any Pr-Co-B alloy was unambiguous evidence of the presence of the $Pr_2Co_{14}B$ phase in the alloy. The TMA cooling curve shows in addition that upon heating the alloy A_1 at ~1000 °C, some of the Pr_2Co_{17} crystals start dissolving and some more $Pr_2Co_{14}B$ crystals are formed. This is indicated by the relative decrease (corresponding to dissolution) or increase (corresponding to formation) of the magnetization during heating and cooling. It can be suggested that, upon heating the as-cast alloy, thermodynamic equilibrium is being established and eventually only the $Pr_2Co_{14}B$ will be present. This is evident in the microstructure and in the corresponding TMA curve (Fig. 17c-d) of alloy A_1 which was isothermally heat treated at 1000 °C. Both show essentially a single-phase alloy of composition $Pr_2Co_{14}B$.

Alloy A_2 of Composition $Pr_{2.89}Co_{95.42}B_{1.69}$. The microstructure of the as-cast alloy A_2 together with its corresponding TMA curve are shown in Fig. 18a-b. In this alloy, the primary αCo solidifies first from the melt as the liquid composition follows the Co-A_2 line. Upon reaching the alteration boundary between the primary solidification phase fields of αCo and Pr_2Co_{17}, a peritectic reaction will occur, where some αCo reacts with the liquid producing the Pr_2Co_{17} crystals:

$$\alpha Co + \text{Liquid} \leftrightarrow Pr_2Co_{17}$$

The peritectic structure is clearly evident in Fig. 18a, where αCo grains are surrounded by the Pr_2Co_{17} phase. The composition of the melt follows the alteration boundary and reaches the point P_1, where a quasi-peritectic reaction occurs producing $Pr_2Co_{14}B$ and αCo crystals:

$$Pr_2Co_{17} + \text{Liquid} \leftrightarrow Pr_2Co_{14}B + \alpha Co$$

This is represented in the microstructure of Fig. 18a by a mixture of $Pr_2Co_{14}B$ and αCo surrounding the Pr_2Co_{17} grains.

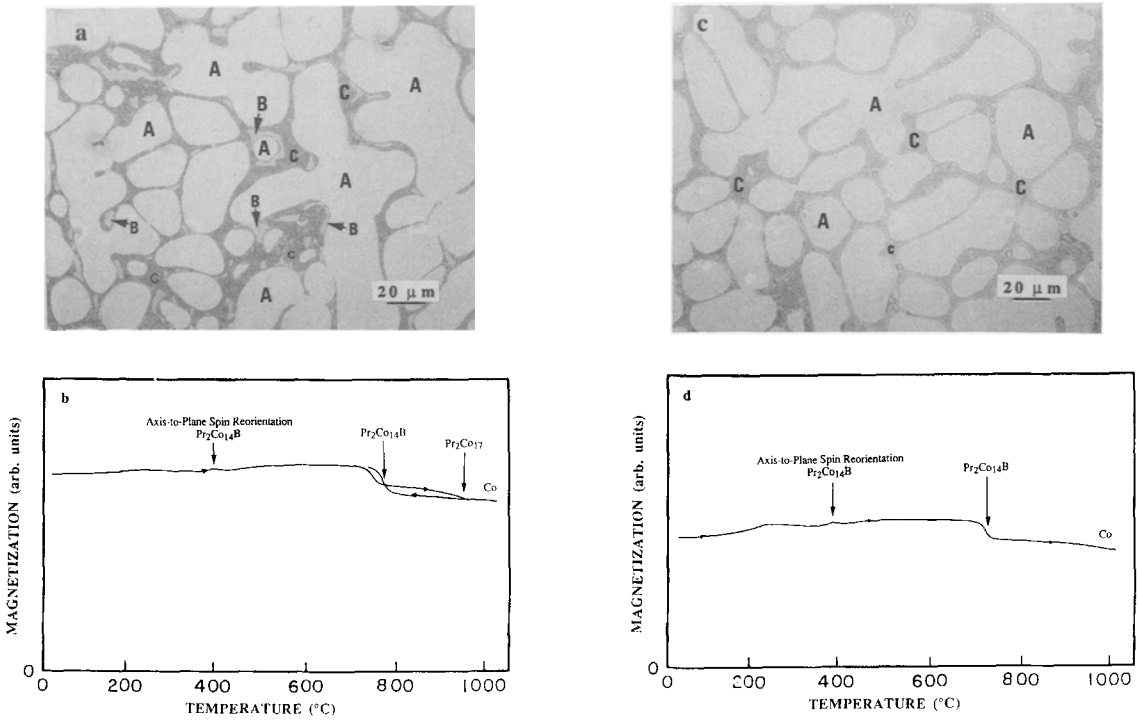

Fig. 18 Microstructure (a) and TMA (b) of the as-cast alloy A_2 ($Pr_{2.89}Co_{95.42}B_{1.69}$). Microstructure (c) and TMA (d) of the alloy A_2 heat treated at 1000 °C. A = Co, B = Pr_2Co_{17}, C = $Pr_2Co_{14}B$.

The TMA heating curve (Fig. 18b) shows that the phases present in the as-cast alloy A_1 are αCo, Pr_2Co_{17}, and $Pr_2Co_{14}B$. The TMA cooling curve shows that upon reaching temperatures ~1000 °C, the Pr_2Co_{17} phase completely dissolves so that the final equilibrium phases present become only αCo and $Pr_2Co_{14}B$. Both the microstructure and TMA curve of the alloy A_2 heat treated isothermally at 1000 °C are shown in Fig. 18c-d. They both indicate the existence of αCo and $Pr_2Co_{14}B$. This result is a consequence of the fact that the composition of alloy A_2 lies on the Co-$Pr_2Co_{14}B$ Alkemade line.

Alloy A_3 of Composition $Pr_6Co_{85}B_9$. The microstructure and corresponding TMA curve of the as-cast alloy A_3 are shown in Fig. 19. The composition of alloy A_3 falls inside the primary solidification phase field of αCo. Hence, the melt of this alloy solidifies along the Co-A_3 line by precipitating the primary αCo. When the remaining liquid reaches the equilibrium boundary between the primary solidification phase field of αCo and $Pr_2Co_{14}B$, secondary precipitation begins. The last liquid solidifies eutectically at E_2 according to the reaction:

$$\text{Liquid} \leftrightarrow Pr_2Co_{14}B + PrCo_{12}B_6 + \alpha Co$$

The ternary eutectic microstructure produced by the above reaction is shown in Fig. 19a. The TMA curve (Fig. 19b) confirms the existence of the three phases: $Pr_2Co_{14}B$, αCo, and $PrCo_{12}B_6$ (T_C = 167 K). As before, the presence of αCo is evident from the observation that, even at the highest reached temperature, the magnetization has a nonzero value because the αCo is still below its Curie temperature.

Alloy A_4 of Composition $Pr_{5.45}Co_{64.55}B_{30}$. The microstructure and corresponding TMA curve of the as-cast alloy A_4 are shown in Fig. 20. Upon solidification in this alloy A_4, the primary $PrCo_{12}B_6$ crystals precipitate while the composition of the liquid moves along the $PrCo_{12}B_6$-A_4 line until the equilibrium boundary of the primary solidification phase field of $Pr_2Co_{14}B$ is reached. At that point, a pseudobinary eutectic mixture of $PrCo_{12}B_6$ and $Pr_2Co_{14}B$ will form from the liquid according to the reaction:

$$\text{Liquid} \leftrightarrow Pr_2Co_{14}B + PrCo_{12}B_6$$

Finally, the composition of the liquid follows the equilibrium boundary towards E_2, where the last liquid solidifies according to the ternary eutectic reaction:

$$\text{Liquid} \leftrightarrow Pr_2Co_{14}B + PrCo_{12}B_6 + \alpha Co$$

Both the binary and ternary eutectic microstructures are clearly seen in Fig. 20a. The TMA curve (Fig. 20b) confirms the existence of phases $Pr_2Co_{14}B$, $PrCo_{12}B_6$, and αCo in the as-cast alloy A_4. The microstructure and corresponding TMA curve of the same alloy that was isothermally heat treated at 1000 °C are shown in Fig. 12. Heat treatment at 1000 °C causes substantial coarsening of the phases present, and the eutectic microstructures are not evident any more.

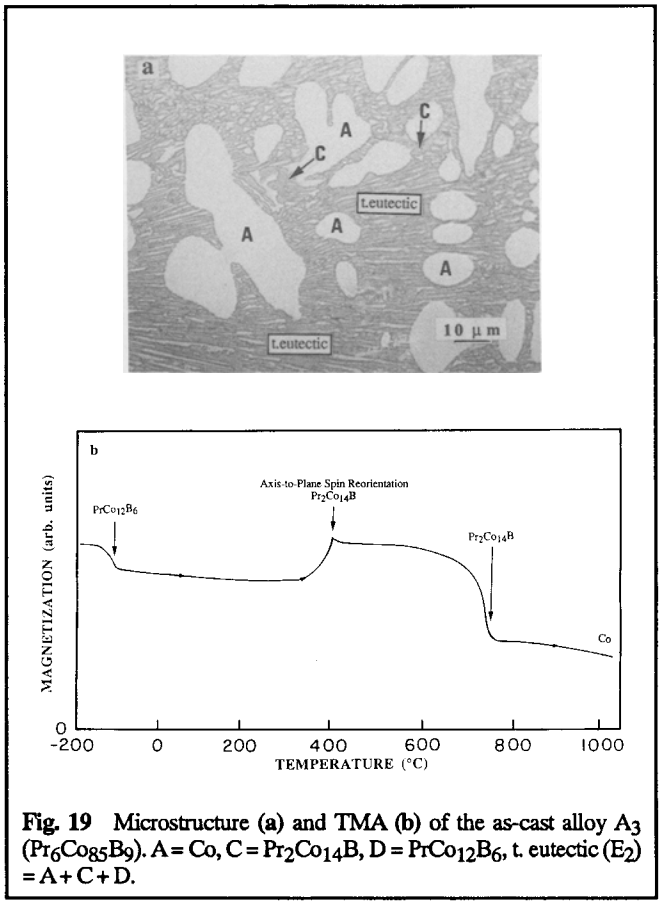

Fig. 19 Microstructure (a) and TMA (b) of the as-cast alloy A_3 ($Pr_6Co_{85}B_9$). A = Co, C = $Pr_2Co_{14}B$, D = $PrCo_{12}B_6$, t. eutectic (E_2) = A + C + D.

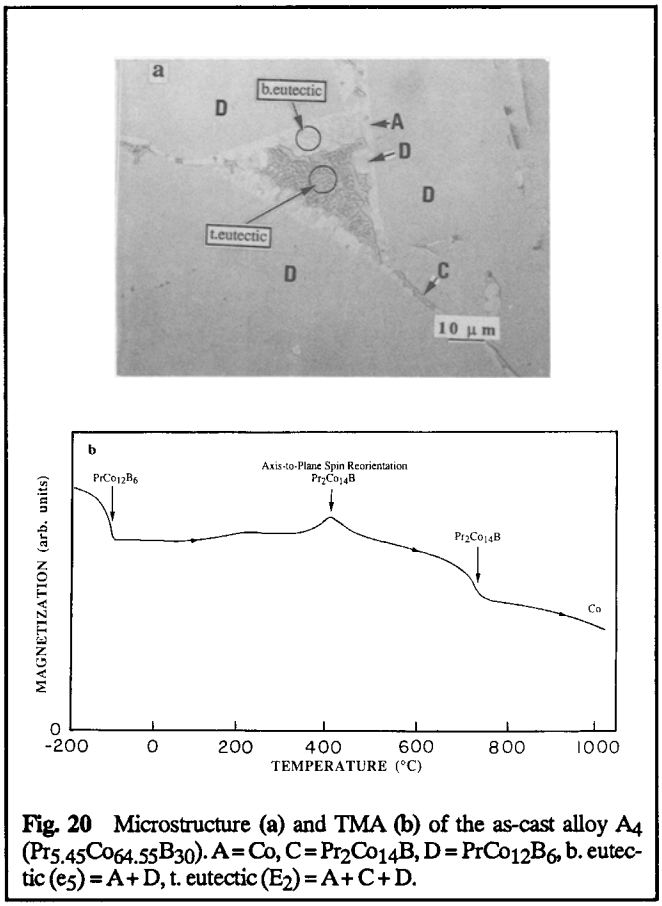

Fig. 20 Microstructure (a) and TMA (b) of the as-cast alloy A_4 ($Pr_{5.45}Co_{64.55}B_{30}$). A = Co, C = $Pr_2Co_{14}B$, D = $PrCo_{12}B_6$, b. eutectic (e_5) = A + D, t. eutectic (E_2) = A + C + D.

Alloy A_5 of Composition $Pr_{12.99}Co_{78.43}B_{8.58}$. The microstructure and corresponding TMA curve of the as-cast alloy A_5 are shown in Fig. 21. The composition of alloy A_5 falls inside the primary solidification phase field of $Pr_2Co_{14}B$. Therefore, the composition of the melt of alloy A_5 follows the $Pr_2Co_{14}B$-A_5 line, by precipitating primary crystals of $Pr_2Co_{14}B$. Finally, the composition of the melt reaches the univariant point e_3, where a pseudobinary eutectic reaction occurs producing $Pr_2Co_{14}B$ and $PrCo_4B$:

$$\text{Liquid} \leftrightarrow Pr_2Co_{14}B + PrCo_4B$$

Both the primary $Pr_2Co_{14}B$ grains and binary ($Pr_2Co_{14}B$ + $PrCo_4B$) eutectic microstructure are shown in Fig. 21a. The TMA curve (Fig. 21b) of the as-cast alloy A_5 confirms the existence of $Pr_2Co_{14}B$ and $PrCo_4B$ phases in this alloy.

5. Discussion

Major differences have been observed between the Fe-Nd-B (and consequently the Fe-Pr-B) and Co-Pr-B phase diagrams. Although in both systems the $R_2TM_{14}B$ phase forms peritectically, in the case of the Co-based system the reaction involves the Pr_2Co_{17} phase rather than the αCo (α-Fe) phase, which is involved in the Fe-based system.[19-24] The primary solidification phase fields surrounding the primary field of $Pr_2Co_{14}B$ are different from those surrounding the $Nd_2Fe_{14}B$ phase. In the case of the Fe-based system, phases, such as $NdFe_{12}B_6$, $NdFe_4B$, and $NdFe_5$, do not exist in stable equilibrium. The primary solidification phase field of $Nd_2Fe_{14}B$ shares a boundary in common with the one of Nd and $NdFe_4B_4$ phases (both phases are not magnetic at room temperature). The three phases—$Nd_2Fe_{14}B$, Nd, and $NdFe_4B_4$—are known to form a low-temperature ternary eutectic. The existence of the ternary eutectic in the Fe-based system is found to be greatly responsible for the increase of the intrinsic coercivity of the $Nd_2Fe_{14}B$-based magnets, which were sintered at ~1080 °C and subsequently annealed near the eutectic temperature (~665 °C). The increase of the intrinsic coercivity is attributed to the change of the microstructure (smoother and defect-free grains) during annealing. Such a low-temperature ternary eutectic does not exist in the Co-based system. The $Pr_2Co_{14}B$-based magnets have to be sintered[1,5] at 1100 °C. The optimal microstructure (smooth and defect-free grains) exhibiting the highest intrinsic coercivity has to be formed directly during sintering. Low-temperature annealing at 600 to 700 °C does not have any effect on the microstructure or the intrinsic coercivity. The lowest temperature ternary eutectic involving the $PrCo_{14}B$ phase is found to be at ~1030 °C (as was found from DTA curves not shown herein). Furthermore, the phases involved (other than the $Pr_2Co_{14}B$ phase) in the two ternary eutectics (E_1 and E_2) are αCo, $PrCo_{12}B_6$, and $PrCo_4B$. Of these, only $PrCo_{12}B_6$ is nonmagnetic at room temperature. The secondary phases present in the Pr_2Co_{14} B-based sintered mag-

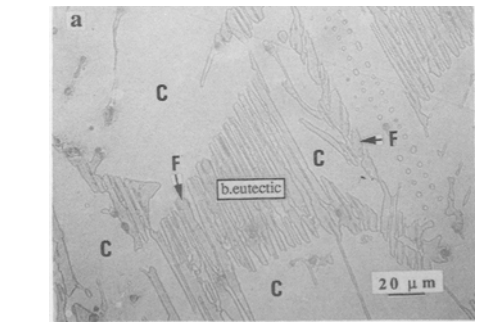

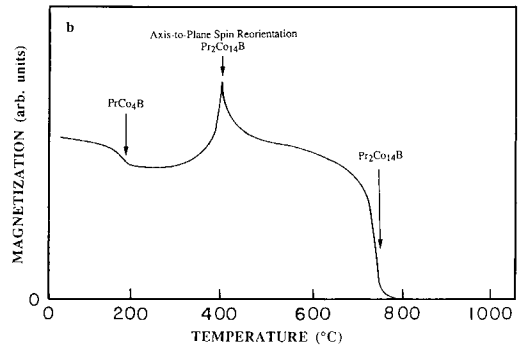

Fig. 21 Microstructure (a) and TMA (b) of the as-cast alloy A_5 ($Pr_{12.99}Co_{78.43}B_{8.58}$). C = $Pr_2Co_{14}B$, F = $PrCo_4B$, b. eutectic = C+F.

nets[1,5] are $PrCo_4B$ and traces of $PrCo_5$ or $PrCo_{12}B_6$. The final composition of such magnets was found to be located very close to the $Pr_2Co_{14}B$-$PrCo_4B$ Alkemade line (see Fig. 5). Depending on the side of the Alkemade line of which the overall magnet composition is located, one can observe the presence of traces of either $PrCo_5$ or $PrCo_{12}B_6$ phases. It is very possible that if one chooses the final composition of the sintered magnets to be located on the $Pr_2Co_{14}B$-$PrCo_{12}B_6$ Alkemade line, the resulting intrinsic coercivity of the magnets will be maximized. This is because the secondary $PrCo_{12}B_6$ phase is nonmagnetic and will effectively isolate the magnetic $Pr_2Co_{14}B$ grains. In the case of the $Pr_2Co_{14}B$-based rapidly quenched magnets,[1] the secondary phases are the $PrCo_4B$ and traces of $PrCo_{12}B_6$. In this case, the composition of the magnets was located inside the compatibility triangle involving the $PrCo_{12}B_6$ and not the $PrCo_5$ phase (left side of the $Pr_2Co_{14}B$-$PrCo_4B$ Alkemade line). Wecker and Schultz[4] considered that the secondary phase present in their rapidly quenched $Pr_2Co_{14}B$-based magnets is $PrCo_2$. This conclusion was based on the reflections observed in their CuK_α X-ray pattern at $2\theta = 34.6°$ and 40.5°. According to the present Co-Pr-B phase diagram, we concluded that the presence of $PrCo_2$ is highly improbable. We believe that the observed reflections are due to the presence of the $PrCo_4B$ phase. This is also supported by the fact that $PrCo_4B$ is a very stable phase and forms a pseudobinary eutectic together with $Pr_2Co_{14}B$. Fuerst *et al.*[2,3] did not report the presence of the $PrCo_4B$ phase in their rapidly quenched magnets, although their published X-ray patterns (CuK_α) in Ref. 2 (Fig. 2) and Ref. 3 (Fig. 3) clearly show the (110) reflection of the $PrCo_4B$ phase at $2\theta = 35°$.

6. Summary

The liquidus projection surface and the isothermal section at 1000 °C of the Co-Pr-B (Co-rich) ternary phase diagram have been determined. Thermomagnetic measurements (TMA) have been employed to determine the phases present in the Co-Pr-B alloys. The "Alkemade lines" and "Alkemade theorem" have been employed to determine the position of the equilibrium phase boundaries and their trend with respect to temperature. The primary solidification phase field of the $Pr_2Co_{14}B$ intermetallic compound is found to share boundaries in common with the primary solidification phase fields of αCo, Pr_2Co_{17}, $PrCo_5$, $PrCo_4B$, and $PrCo_{12}B_6$ intermetallics. The reaction through which the $Pr_2Co_{14}B$ forms is the pseudobinary peritectic reaction Pr_2Co_{17} + Liquid ↔ $Pr_2Co_{14}B$.

The obtained information about the Co-Pr-B phase diagram was used to explain correctly all the phases present in the $Pr_2Co_{14}B$-based permanent magnets. The major phases present in these magnets (other than $Pr_2Co_{14}B$) are the $PrCo_4B$ and $PrCo_{12}B_6$ or $PrCo_5$ depending on the overall composition of the magnet alloy. Also, it has been shown that the features (*i.e.*, ternary eutectics) of the Co-Pr-B ternary phase diagram are different from those of the Fe-Nd-B and consequently of the Fe-Pr-B phase diagram. That explains the fact that the experimental conditions used for the preparation of the $Nd_2Fe_{14}B$ or $Pr_2Fe_{14}B$ based magnets (sintering at 1080 °C plus annealing at 600 to 700 °C) are different from those used in the case of the $Pr_2Co_{14}B$-based magnets (only sintering at 1100 °C). The different kind of phases present in the microstructure of these magnets is also attributed to the differences in their respective phase diagrams.

Appendix

A straight line connecting the points representing the compositions of the (stoichiometric) phases in a ternary system is called a binary join. A binary join connecting the compositions of two phases for which the primary solidification phase fields have a common boundary line is called an Alkemade line. Alkemade lines divide a ternary diagram into compatibility triangles. A compatibility triangle is always made up of three Alkemade lines. Also note that Alkemade lines never cross one another. When cooled to solidification under equilibrium conditions, any melt whose composition falls within a compatibility triangle will tend to form a combination of phases indicated at the apexes of the compatibility triangle. If three phases form a compatibility triangle, then their primary phase fields share a common boundary. The Alkemade theorem states that the intersection of a boundary line (or boundary line extended) with its corresponding Alkemade line (or Alkemade line extended) represents a temperature maximum on that boundary line and a temperature minimum on the Alkemade line. The Alkemade theorem permits one to analyze the direction of the slope of

boundary lines with respect to temperature and to determine the general trend in the shape of the liquidus surface. For further information, please consult Ref. 40 and 41.

Acknowledgment

This work was supported by the Magnetic Materials Research Group at Carnegie Mellon University, funded by grant No. DMR 8613386 from the National Science Foundation, Washington, DC, which is gratefully acknowledged.

Cited References

1. C.N. Christodoulou, "Magnetic and Metallurgical Characteristics of the Pr-Co-B (Co-Rich) Ternary System," Ph.D. Dissertation, Carnegie Institute of Technology, Carnegie Mellon University, Pittsburgh, PA, USA (Apr 1990).
2. C.D. Fuerst, J.F. Herbst, and F.E. Pinkerton, *J. Appl. Phys.*, *64*, 5556 (1988).
3. C.D. Fuerst and J.F. Herbst, *J. Appl. Phys.*, *64*, 1332 (1988).
4. J. Wecker and L. Schultz, *Appl. Phys. Lett.*, *54*, 393 (1989).
5. C.N. Christodoulou, W.E. Wallace, and T.B. Massalski, *J. Appl. Phys.*, *66*, 2749 (1989).
6. N.S. Bilonizhko and Yu.B. Kuz'ma, *Izv. Akad. Nauk SSSR, Neorg. Mater.*, *10*, 265 (1974).
7. Yu.B. Kuz'ma and G.F. Stepanchikova, *Izv. Akad. Nauk SSSR, Neorg. Mater.*, *10*, 2223 (1974).
8. G.F. Stepanchikova and Yu.B. Kuz'ma, *Vestn.-Lvov Univ., Ser. Khim.*, *18*, 16 (1976).
9. N.F. Chaban and Yu.B. Kuz'ma, *Izv. Akad. Nauk SSSR, Neorg. Mater.*, *13*, 923 (1977).
10. H.H. Stadelmaier and H.J. Lee, *Z. Metallkd.*, *69*, 685 (1978).
11. N.S. Bilonizhko, Yu.B. Kuz'ma, and L.D. Polyanaskaya, *Izv. Akad. Nauk SSSR, Neorg. Mater.*, *16*, 832 (1980).
12. N.A. El Masry and H.H. Stadelmaier, *J. Less-Common Met.*, *96*, 165 (1984).
13. N.S. Bilonizhko and Yu.B. Kuz'ma, *Izv. Akad. Nauk SSSR, Neorg. Mater.*, *19*, 487 (1983).
14. G.V. Chernyak, N.F. Chaban, and Yu.B. Kuz'ma, *Izv. Akad. Nauk SSSR, Neorg. Mater.*, *19*, 1757 (1983).
15. O.M. Lub, N.F. Chaban, and Yu.B. Kuz'ma, *Poroshk. Metall.*, *10*, 82 (1988).
16. N.S. Bilonizhko, L.V. Leshko, and Yu.B. Kuz'ma, *Izv. Akad. Nauk SSSR, Neorg. Mater.*, *21*, 1798 (1985).
17. Y.C. Chuang, C.H. Wu, and F.H. Wang, *J. Less-Common Met.*, *135*, 5 (1987).
18. Y.C. Chuang, C.H. Wu, and F.H. Wang, *Proceedings of the 5th International Symposium on Magnetic Anisotropy and Coercivity in Rare Earth-Transition Metal Alloys*, BadSoden, FRG, p. 439, Sept. 3, 1987.
19. H.H. Stadelmaier, N.A. Elmasry, N.C. Liu, and S.F. Sheng, *Mater. Lett.*, *2*, 411 (1984).
20. Y. Matsuura, S. Hirosawa, H. Yamamoto, S. Fujimura, M. Sagawa, and K. Osamura, *Jpn. J. Appl. Phys.*, *24*, L635 (1985).
21. K.H.J. Buschow, D.B. de Mooij, and H.M. van Noort, *Philips J. Res.*, *40*, 227 (1985).
22. K.H.J. Buschow, D.B. de Mooij, J.L. Damms, and H.M. van Noort, *J. Less-Common Met.*, *115*, 357 (1986).
23. G. Schneider, E.T. Henig, G. Petzow, and H.H. Stadelmaier, *Z. Metallkd.*, *77*, 755 (1986).
24. E.T. Henig, G.S. Schneider, and H.H. Stadelmaier, *Z. Metallkd.*, *78*, 818 (1987).
25. T.B. Massalski, J.L. Murray, L.H. Bennett, and H. Baker, *Binary Alloy Phase Diagrams*, Vol. 1 and 2, American Society for Metals, Metals Park, OH (1986).
26. Y. Khan, *Acta Crystallogr.*, *830*, 1533 (1974).
27. Y. Khan, *Phys. Status Solidi (a)*, *23*, 425 (1974).
28. Y. Khan and D. Feldmann, *J. Less-Common Met.*, *33*, 305 (1973).
29. K.H.J. Buschow, *Pep. Prog. Phys.*, *40*, 1179 (1977).
30. Y. Khan, *Z. Metallkd.*, *65*, 489 (1974).
31. W.B. Pearson, *The Crystal Chemistry and Physics of Metals and Alloys*, Wiley-Interscience, New York (1972).
32. K.H.J. Buschow, D.B. de Mooij, S. Sinnema, R.J. Radwanski, and J.J.M. France, *J. Magn. Magn. Mat.*, *52*, 211 (1985).
33. A.T. Pedziwiatr, H.Y. Chen, W.E. Wallace, and S.K. Malik, *IEEE Trans. Magn. MAG-23*, 2717 (1987).
34. Yu.B. Kuz'ma and N.S. Bilonizhko, *Kristallografiya*, *18*, 710 (1973).
35. Yu.B. Kuz'ma, N.S. Bilonizhko, S.I. Mykhalenko, G.F. Stepanchikova, and N.F. Chaban, *J. Less-Common Met.*, *67*, 51 (1979).
36. M. Jurczyk, A.T. Penziwiatr, and W.E. Wallace, *J. Magn. Magn. Mat.*, *67*, L1 (1987).
37. A.T. Penziwiatr, S.Y. Jiang, W.E. Wallace, E. Burzo, and V. Pop, *J. Magn. Magn. Mat.*, *66*, 99 (1987).
38. Yu.B. Kuz'ma, G.V. Chernjak, and N.F. Chaban, *Dop. Akad. Ukr. RAR*, *A*(12), 80 (1981).
39. Y.C. Chuang, C.H. Wu, T.D. Chang, F.H. Wang, and F.R. De Boer, *J. Less-Common Met.*, *144*, 249 (1988).
40. G.A. Rankin and F.E. Wright, *Am. J. Sci. 4th Ser.*, *39*, 18 (1915).
41. C.G. Bergeron and S.H. Risbud, *Introduction to Phase Equilibria in Ceramics*, The American Ceramic Society, Inc., Westerville, OH (1984).